## Simulating Microwave Radiation of Pyramidal Horn Antenna for Plasma Diagnostics

J. S. Shang\*

Mechanical and Material Engineering Department, Wright State University, Dayton Ohio 45435, USA.

Recevied 13 September 2005; Accepted (in revised version) 5 December 2005 Communicated by Wei Cai

Abstract. Computational simulation of the radiating structure of a microwave from a pyramidal horn has been successfully accomplished. This simulation capability is developed for plasma diagnostics based on a combination of three-dimensional Maxwell equations in the time domain and the generalized Ohm's law. The transverse electrical electromagnetic wave of the  ${\rm TE}_{1,0}$  mode propagating through a plasma medium and transmitting from antenna is simulated by solving these governing equations. Numerical results were obtained for a range of plasma transport properties including electrical conductivity, permittivity, and plasma frequency. As a guided microwave passing through plasma of finite thickness, the reflections at the media interfaces exhibit substantial distortion of the electromagnetic field within the thin sheet. In radiating simulation, the edge diffraction at the antenna aperture is consistently captured by numerical solutions and reveals significant perturbation to the emitting microwave. The numerical solution reaffirms the observation that the depth of the plasma is a critical parameter for diagnostics measurement.

Key words: Plasma diagnostics; microwave simulation; antenna.

#### 1 Introduction

Recently magneto-fluid-dynamics has become the most vibrant research topic in the aerospace science community through an added physical dimension for enhancing aerodynamic performance of flight vehicles. In this aspect, magneto-fluid-dynamics reemerges as one of the few last frontiers for fluid dynamic research [1,2]. Magneto-aerodynamic interactions have been widely applied and have demonstrated impressive application potential

<sup>\*</sup>Correspondence to: J. S. Shang, Mechanical and Material Engineering Department, Wright State University, Dayton Ohio 45435, USA. Email: Joseph.shang@wright.edu

for flow control [3–7], MHD scramjet bypass [8], innovative radiatively drive hypersonic wind tunnel [9] and combustion or ignition enhancement [10]. To accurately assess the relative magnitude of electromagnetic and aerodynamic forces in an interaction, an accurate evaluation of the plasma transport properties such as the charge particle number density, temperatures and electric conductivity become necessary.

Partially ionized plasma or weakly ionized air in aerospace applications has a distinctive oscillatory and instability feature. Therefore, all experimental measurement techniques must be able to determine the characteristics of these oscillations and to provide sufficient resolution to this important aspect of the experiment [11–13]. Plasma exhibits outstanding attributes at different thermodynamic states. The high-temperature plasma radiates electromagnetic waves over a broad frequency spectrum ranging from microwaves to the infrared, ultraviolet, and X-ray regions. These radiations result from the bound-bound (atoms or ions), free-bound (electron-ion recombination), free-free transitions (elastic collisions of charged particles with atoms, bremsstrahlung), and in the presence of a strong magnetic field the radiation even emits from electrons spinning [14]. For plasma diagnostics using radiation, spectral line intensity measurements have been extensively used by most traditional methods. The comparative measurements of spectral line intensities have also been used to determine the electron temperature in low-temperature plasma [15, 16].

A widely used non-intrusive plasma diagnostic tool is microwave probing. The microwave system is adopted both for plasma diagnostics and in deep-space communication. For plasma diagnostics, the number density of the charge particles and its collision frequency with the neutral particles are measured based on the microwave attenuation phenomenon [17–20]. This unique microwave behavior in weakly ionized air is also known for the famous communication blackout phenomenon in the reentry phase either for an aerospace vehicle or for an inter-planet flight [21, 22]. Communication blackout is the consequence of an incident microwave propagating at a frequency lower than the cut-off frequency [23]. When the two frequencies equal, the propagating wave starts to become evanescent and the transmission of the electromagnetic energy ceases. When the transmission bandwidth is greater than that of the plasma, the microwave will attenuate as it propagates through the plasma. The dissipated energy along the wave path is proportional to the electrical conductivity of the medium.

An electromagnetic wave propagating in an electrically conducting medium depends strongly on its electrical conductivity and the transmission frequency. For a linear polarized plane wave traveling in a conducting medium, the current density consists of the conductive and displacement components. For an electrically neutral medium, the electric conductivity  $\sigma$  and the conductive current vanish, and the wave may travel without any impedance. Otherwise, the relative magnitude of  $\sigma$  and the product of wave frequency and electrical permittivity  $\omega \varepsilon$  will dominate the behavior of the propagating wave [23]. In the absence of an external magnetic field, the partially ionized gas can be studied as an isotropic medium. The plasma behaves as a simple quasi conductor and will support high frequency wave motion through the response of electrons.

This salient feature of microwave attenuation in plasma has been used to measure the

plasma transport property of a rocket exhaust plume [17–19] and the weakly ionized air stream in a hypersonic wind tunnel [15,16,20]. For plasma diagnostics, added complication arises when a microwave impinges on a boundary of two media. At the interface, a part of the incident wave is reflected and another part is transmitted into the second medium. The portion of the transmitted wave is governed by the continuity of the tangential components of electric and magnetic field. The intrinsic impedance of the media ultimately controls the behavior of this electromagnetic field at the interface [23]. For a plane wave traveling in air impacts normally to a perfect conductor, the incident magnetic field doubles its intensity at the media interface. On the exit interface, the electric field can also double its strength at the boundary. In both cases, a standing wave originates at the boundary. In all circumstances, there will be a reflected wave from the interface, except when the two media have the identical impedance, and then the incident wave will transmit uninterrupted.

In most microwave probing, the wave produced by the generator is directed by a waveguide and transmitted from an antenna; the basic arrangement is depicted in Fig. 1 [11, 12]. The widely used antennae usually are a pair of pyramidal horns whose main function is to collimate the wave and reduce diffraction. The behavior of these components in plasma diagnostics is also the least understood. For this reason, some fundamental and data accuracy uncertainty for plasma diagnostics remains [11,12]. The evidence is clearly demonstrated by independent measurements using Langmuir probe [24] and microwave absorption techniques [20]. The measurement discrepancy on charged number density of a direct current glow discharge in a hypersonic stream is greater than a factor of two and in practical applications the difference can be as high as one order-of-magnitude. The sources of data disparity are many; they include the explicit assumptions of the outer boundary of the plasma and diffraction/refraction of the microwave. Even for a simple glow discharge simulation, these simplifying assumptions of a weakly ionized gas are seriously challenged [25, 26]. It is therefore natural to explore a numerical simulation technique to obtain a better understanding for the basics of microwave diagnostics.

The present investigation will detail the development of a numerical simulation capability for electromagnetic wave radiation and propagation in a weakly ionized gas. Specifically, the microwave beam path from a pyramidal horn across the interface of air and weakly ionized gas will be formulated, simulated, and validated by comparing with available theoretical and experimental results.

## 2 Governing equations

The simulation capability for plasma microwave diagnostics is a multi-disciplinary endeavor in which the interactions between electromagnetic, fluid dynamics, and chemical kinetics are required. For flow control using plasma actuators, the electron collision process is the preferred mechanism for plasma generation via a direct (DC) or alternative current (AC) high voltage power supply or radio frequency radiation. Under this circumstance, ionization and recombination are far from thermodynamic equilibrium. Some of the re-

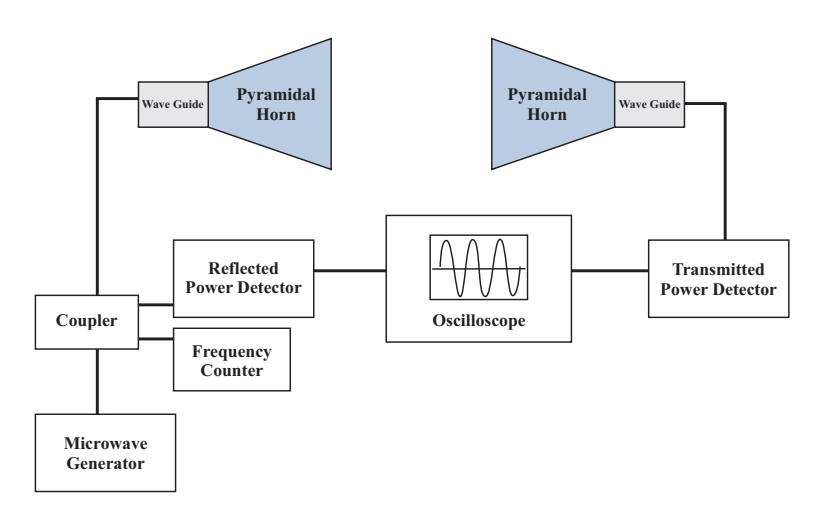


Figure 1: Experimental setup of microwave absorption measurement.

quired knowledge in these disciplines is known only at the phenomenological level, the fidelity to physics is thus uncertain [1,2]. In fact, the sole description of low-temperature plasma is based on drift-diffusion theory. The complex chemical kinetics and electrodynamics phenomena are governed by the classic Thompson coefficient [14]. To alleviate these presently irresolvable complexities, the non-equilibrium chemical kinetics is not included in the present formulation. This approximation is justified by the fact that the charged particles, electrons and ions, are presented only in a trace amount of mass fraction  $-10^{-6}$  [3–7, 15, 16]. The partial ionized gas is thereby treated as an isotropic and homogeneous lossy medium. The validating range of the present approach will be assessed and delineated by a build-up process [21,22].

For the application range of microwave diagnostics, the plasma encountered is mostly in the so-called ideal classical domain. According to the classification by charged particle number density and electron temperature, the thermal kinetic energy is large in comparison with Coulomb interaction energy,  $k_bT\gg e^2/n^{-1/3}$  in this domain. This condition is equivalent to n  $\lambda_D^3\gg 1$ , where  $\lambda_D$  is the Debye length, and the weak interaction model prevails. Therefore, the loose coupling of the Maxwell, Navier-Stokes and generalized Ohm equations shall be an appropriate formulation to analyze the dominant physical phenomena.

The present analysis is focused on the development of a numerical simulation capability for microwave radiation from a pyramidal horn. From this physics-based simulation, the edge diffraction at the horn exit and the microwave interference during the wave emission can be assessed. At the same time, the attenuation of a microwave that propagates through plasma is computed for a range of electric conductivities, plasma frequencies, and electric permittivities  $\sigma/\omega\varepsilon$ .

The governing equations for the present effort are built around the solution to the threedimensional Maxwell equations in the time domain. The closure of the partial differential equation system requires additional constitutive relationships to describe the electrical current, J, and charge density,  $\rho_e$ . The rate of change of the electrical charge density is derived from the generalized Ohm's law. The kinetic foundation of a many-component model for the partially ionized gas is the Boltzmann equation [27,28]. In a dilute gas, the collision terms in the equation are short range, so the contribution of the intermolecular collisions is practically instantaneous and localized at a point in space. However, there is no unique formulation to bridge the microscopic and the macroscopic quantity, the present analysis adopts the following approximation [27]:

$$(1/\varpi_{eh})\partial \mathbf{J}/\partial t - \sigma \mathbf{E} + \mathbf{J} = 0, \tag{2.1}$$

where  $\varpi_{eh}$  is the average collision frequency between electrons and heavy particles and  $\sigma$  is the electrical conductivity,  $\sigma = n_e e^2/m_e \nu$ . The governing equations are built around the solution to the three-dimensional Maxwell equations in the time domain. The closure of the partial differential equation system requires additional constitutive relationships to describe the electrical current, J, and charge density,  $\rho_e$ . Like a chain reaction, once the generalized Ohm's equation is included to relate the electric field strength with current density, additional information of kinematic and thermodynamic properties of the flow field are required. However based on the previous discussion, the genetic form of the governing equations remains unaltered [21–23].

$$\partial \mathbf{B}/\partial t + \nabla \times \mathbf{E} = 0, \tag{2.2}$$

$$\partial \mathbf{D}/\partial t - \nabla \times \mathbf{H} = -\mathbf{J}, \tag{2.3}$$

$$\nabla \cdot \mathbf{B} = 0, \tag{2.4}$$

$$\nabla \cdot \mathbf{D} = \rho_e. \tag{2.5}$$

For the present investigation, the two Gauss's laws, equations (2.4) and (2.5), are automatically satisfied, because the solution is a homogeneous function and the net charged particles number density vanishes in the medium. The global electrically neutral property of the plasma ensures the second constraint. The two divergence equations are therefore eliminated from the present solving scheme [23].

The governing equations cast into the flux vector form in a generalized curvilinear coordinates becomes:

$$\partial \mathbf{U}/\partial t + \partial \mathbf{F}_{\varepsilon}/\partial \varepsilon + \partial \mathbf{F}_{\eta}/\partial \eta + \partial \mathbf{F}_{\zeta}/\partial \xi = -\mathbf{J}, \tag{2.6}$$

where  $\varepsilon_x$ ,  $\eta_y$ ,  $\zeta_z$  etc are the metrics of coordinate transformation from the Cartesian (x, y, z) to a generalized curvilinear, body-oriented coordinate system  $(\varepsilon, \eta, \zeta)$ . The components of the flux vector in the transformed coordinates are:  $\mathbf{F}_{\varepsilon} = \mathbf{F}_{\varepsilon}(\varepsilon_x F_x, \varepsilon_y F_y, \varepsilon_z F_z)$ ,  $\mathbf{F}_{\eta} = \mathbf{F}_{\eta}(\eta_x F_x, \eta_y F_y, \eta_z F_z)$ , and  $\mathbf{F}_{\zeta} = \mathbf{F}_{\zeta}(\zeta_x F_x, \zeta_y F_y, \zeta_z F_z)$ . Since the three components are similar, only the component in  $\xi$  coordinate is given in here.

$$\mathbf{F}_{\xi} = \begin{pmatrix} 0 & 0 & 0 & 0 & -\xi_z/j\varepsilon & \xi_z/j\varepsilon \\ 0 & 0 & 0 & 0 & \xi_z/j\varepsilon & 0 & -\xi_x/j\varepsilon \\ 0 & 0 & 0 & -\xi_y/j\varepsilon & \xi_x/j\varepsilon & 0 \\ 0 & \xi_z/j\mu & \xi_y/j\mu & 0 & 0 & 0 \\ -\xi_z/j\mu & 0 & \xi_x/j\mu & 0 & 0 & 0 \\ \xi_y/j\mu & -\xi_x/j\mu & 0 & 0 & 0 & 0 \end{pmatrix} \begin{pmatrix} B_x \\ B_y \\ B_z \\ D_x \\ D_y \\ D_z \end{pmatrix},$$

where j is the jacobian of coordinate transformation [29, 30].

The above differential system consists of a total of 6 dependent variables and 2 explicit constitutive relations. For the initial/boundary value problem, the initial value can be easily prescribed by theoretical results of the transverse electrical wave in the fundamental mode,  $TE_{1,0}$  as entrance conditions for either the waveguide or the antenna [21,22]. The far field boundary conditions are implemented through the split flux vector formulation to honor the domain of dependence [29]. In essence, at the boundaries of the computational domain, all incoming waves are suppressed using the signs of the local eigenvalue as the discriminator. On the electrically conducting surface of the waveguide and antenna, the tangential components of the electric field strength E, and the normal components of the magnetic flux density B, are continuous across the boundary. The discontinuity of the tangential components of magnetic field strength H is equal to the surface density  $J_s$ . Finally the surface charge density  $\rho_s$ , balances the difference between normal components of the electrical displacement D, across the media interface:

$$n \times (\mathbf{E}_1 - \mathbf{E}_2) = 0, \tag{2.7}$$

$$n \times (\mathbf{H}_1 - \mathbf{H}_2) = J_s, \tag{2.8}$$

$$n \cdot (\mathbf{B}_1 - \mathbf{B}_2) = 0, \tag{2.9}$$

$$n \cdot (\mathbf{D}_1 - \mathbf{D}_2) = \rho_s. \tag{2.10}$$

A high-resolution, cell-centered, finite-volume algorithm is adopted for now to assess the validity of the system of governing equations including the initial and boundary conditions [21, 22, 29]. The governing equations in discrete space are:

$$\Delta \mathbf{U}/\Delta t + \Delta \mathbf{F}_{\varepsilon}/\Delta \varepsilon + \Delta \mathbf{F}_{\eta}/\Delta \eta + \Delta \mathbf{F}_{\zeta}/\Delta \zeta = -\mathbf{J}. \tag{2.11}$$

For the hyperbolic partial differential equations system, the governing equations are easily solved by a finite-volume, splitting flux vector scheme. The flux splitting technique is applicable as long as the collision frequency between charged particles is higher than the microwave frequency. Under this circumstance, equation (2.1) reduces to the most basic generalized Ohm's law, which holds for partially ionized plasma [27,28], and the eigenvector structure of the Maxwell equation remains unaltered [21,23,29]. For the pure initial value problem a domain of influence bounded by characteristics exists and reflects the wave-dominant physics. The direction of wave propagation is governed by the eigenvalue and

eigenvector structure. The split flux vectors F<sup>+</sup> and F<sup>-</sup> are uniquely associated with the signs of the eigenvalues of the flux Jacobain matrix,  $\partial \mathbf{F}/\partial \mathbf{U}$ . Physically, this procedure reflects the direction of signature propagation, or the right or left running wave in the domain of dependence. The split vectors on the control surface are reconstructed according to the signs of the eigenvalue to appear as

$$\mathbf{F}_{\varepsilon} = [S_{\xi}(\mathbf{U})(\lambda_{\xi}^{+} + \lambda_{\xi}^{-})S_{\xi}^{-1}(\mathbf{U})] = \mathbf{F}_{\varepsilon}^{+}(\mathbf{U}_{L}) + \mathbf{F}_{\varepsilon}^{-}(\mathbf{U}_{R}),$$

$$\mathbf{F}_{\eta} = [S_{\eta}(\mathbf{U})(\lambda_{\eta}^{+} + \lambda_{\eta}^{-})S_{\eta}^{-1}(\mathbf{U})] = \mathbf{F}_{\eta}^{+}(\mathbf{U}_{L}) + \mathbf{F}_{\eta}^{-}(\mathbf{U}_{R}),$$

$$\mathbf{F}_{\zeta} = [S_{\zeta}(\mathbf{U})(\lambda_{\zeta}^{+} + \lambda_{\zeta}^{-})S_{\zeta}^{-1}(\mathbf{U})] = \mathbf{F}_{\zeta}^{+}(\mathbf{U}_{L}) + \mathbf{F}_{\zeta}^{-}(\mathbf{U}_{R}).$$
(2.12)

In the above equation;  $\lambda_{\xi}$ ,  $\lambda_{\eta}$ , and  $\lambda_{\zeta}$  are the eigenvalues in the transformed space ( $\xi$ ,  $\eta, \zeta$ ). The detailed structure of the similarity matrices and their left-hand inverse of diagonalization, **S** and  $S^{-1}$  can be found in reference [29, 30]. The split flux vectors are finally obtained by a straightforward matrix multiplication,

$$\mathbf{F}^{+} = \mathbf{S}\lambda^{+}\mathbf{S}^{-1} = \mathbf{C}^{+}(\mathbf{U})^{T},$$

$$\mathbf{F}^{-} = \mathbf{S}\lambda^{-}\mathbf{S}^{-1} = \mathbf{C}^{-}(\mathbf{U})^{T},$$
(2.13)

$$\mathbf{F}^{-} = \mathbf{S}\lambda^{-}\mathbf{S}^{-1} = \mathbf{C}^{-}(\mathbf{U})^{T},\tag{2.14}$$

where  $\mathbf{C}^+$  and  $\mathbf{C}^-$  are the coefficient matrices of the split vectors  $\mathbf{F}^+$  and  $\mathbf{F}^-$ , respectively,  $\mathbf{U}^T$  is the transpose of the dependent variables  $(\mathbf{B}_x, \mathbf{B}_y, \mathbf{B}_z, \mathbf{D}_x, \mathbf{D}_y, \mathbf{D}_y)$ . For the present purpose, only the split coefficient matrices in t- $\zeta$  plane are presented:

$$\mathbf{C}_{\zeta}^{+} = \tag{2.15}$$
 
$$\begin{pmatrix} (\zeta_{y}^{2} + \zeta_{z}^{2})/2\gamma\sqrt{\varepsilon\mu} & -\zeta_{x}\zeta_{y}/2\gamma\sqrt{\varepsilon\mu} & 0 & -\zeta_{z}/2\varepsilon & \zeta_{y}/2\varepsilon \\ -\zeta_{x}\zeta_{y}/2\gamma\sqrt{\varepsilon\mu} & (\zeta_{x}^{2} + \zeta_{z}^{2})/2\gamma\sqrt{\varepsilon\mu} & -\zeta_{y}\zeta_{z}/2\gamma\sqrt{\varepsilon\mu} & \zeta_{z}/2\varepsilon & 0 & -\zeta_{x}/2\varepsilon \\ -\zeta_{x}\zeta_{z}/2\gamma\sqrt{\varepsilon\mu} & -\zeta_{y}\zeta_{z}/2\gamma\sqrt{\varepsilon\mu} & (\zeta_{x}^{2} + \zeta_{y}^{2})/2\gamma\sqrt{\varepsilon\mu} & -\zeta_{y}/2\varepsilon & \zeta_{x}/2\varepsilon & 0 \\ 0 & \zeta_{z}/2\mu & -\zeta_{y}/2\mu & (\zeta_{y}^{2} + \zeta_{z}^{2})/2\gamma\sqrt{\varepsilon\mu} & -\zeta_{x}\zeta_{y}/2\gamma\sqrt{\varepsilon\mu} & -\zeta_{x}\zeta_{z}/2\gamma\sqrt{\varepsilon\mu} \\ -\zeta_{z}/2\mu & 0 & \zeta_{x}/2\mu & -\zeta_{x}\zeta_{y}/2\gamma\sqrt{\varepsilon\mu} & (\zeta_{x}^{2} + \zeta_{z}^{2})/2\gamma\sqrt{\varepsilon\mu} & -\zeta_{y}\zeta_{z}/2\gamma\sqrt{\varepsilon\mu} \\ \zeta_{y}/2\mu & -\zeta_{x}/2\mu & 0 & -\zeta_{x}\zeta_{z}/2\gamma\sqrt{\varepsilon\mu} & -\zeta_{y}\zeta_{z}/2\gamma\sqrt{\varepsilon\mu} & (\zeta_{x}^{2} + \zeta_{y}^{2})/2\gamma\sqrt{\varepsilon\mu} \end{pmatrix},$$

$$\mathbf{C}_{\zeta}^{-} = \tag{2.16}$$
 
$$\begin{pmatrix} -(\zeta_{y}^{2} + \zeta_{z}^{2})/2\gamma\sqrt{\varepsilon\mu} & \zeta_{x}\zeta_{y}/2\gamma\sqrt{\varepsilon\mu} & \zeta_{x}\zeta_{z}/2\gamma\sqrt{\varepsilon\mu} & 0 & -\zeta_{z}/2\varepsilon & \zeta_{y}/2\varepsilon \\ \zeta_{x}\zeta_{y}/2\gamma\sqrt{\varepsilon\mu} & -(\zeta_{x}^{2} + \zeta_{z}^{2})/2\gamma\sqrt{\varepsilon\mu} & \zeta_{y}\zeta_{z}/2\gamma\sqrt{\varepsilon\mu} & \zeta_{z}/2\varepsilon & 0 & -\zeta_{x}/2\varepsilon \\ \zeta_{x}\zeta_{z}/2\gamma\sqrt{\varepsilon\mu} & \zeta_{y}\zeta_{z}/2\gamma\sqrt{\varepsilon\mu} & -(\zeta_{x}^{2} + \zeta_{y}^{2})/2\gamma\sqrt{\varepsilon\mu} & -\zeta_{y}/2\varepsilon & \zeta_{x}/2\varepsilon & 0 \\ 0 & \zeta_{z}/2\mu & -\zeta_{y}/2\mu & -(\zeta_{y}^{2} + \zeta_{z}^{2})/2\gamma\sqrt{\varepsilon\mu} & \zeta_{x}\zeta_{y}/2\gamma\sqrt{\varepsilon\mu} & \zeta_{x}\zeta_{z}/2\gamma\sqrt{\varepsilon\mu} \\ -\zeta_{z}/2\mu & 0 & \zeta_{x}/2\mu & \zeta_{x}\zeta_{y}/2\gamma\sqrt{\varepsilon\mu} & -(\zeta_{x}^{2} + \zeta_{z}^{2})/2\gamma\sqrt{\varepsilon\mu} & \zeta_{y}\zeta_{z}/2\gamma\sqrt{\varepsilon\mu} \\ \zeta_{y}/2\mu & -\zeta_{x}/2\mu & 0 & \zeta_{x}\zeta_{z}/2\gamma\sqrt{\varepsilon\mu} & \zeta_{y}\zeta_{z}/2\gamma\sqrt{\varepsilon\mu} & -(\zeta_{x}^{2} + \zeta_{y}^{2})/2\gamma\sqrt{\varepsilon\mu} \end{pmatrix}.$$
 In the above formulation  $\gamma$  is  $(\zeta_{x}^{2} + \zeta_{y}^{2} + \zeta_{z}^{2})^{1/2}$ . The split flux of the three-dimensional

In the above formulation  $\gamma$  is  $(\zeta_x^2 + \zeta_y^2 + \zeta_z^2)^{1/2}$ . The split flux of the three-dimensional Maxwell equations is not unique, but the sum of the split components must be unambiguously identical the flux vector of the governing equation. The split fluxes are solved by a windward biased scheme to honor the zone of dependence. This formulation is essentially an approximate Riemann problem [29]. Meanwhile, the eigenvectors are selected in such a fashion that the matrices of the similarity transformation will degenerate to the form on the Cartesian frame. For the approximate Riemann problem, the three-dimensional problem is first split into three one-dimensional systems, and then the coefficient matrices can be diagonalized in each spatial dimension individually. Finally, the flux vectors in each coordinate are further split according to the signs of the associated eigenvalue or the directions of wave propagation [29, 30].

A third-order spatial resolution is achieved through the reconstruction process of the outward normal flux vectors on control surfaces of the elementary volume. The reconstructed flux vector is balanced on the control surface of the elementary cell to satisfy the governing equations. The specific formulation of the reconstruction process also determines the spatial resolution [21, 22, 29, 30]. The left-  $(\mathbf{U}_L)$  and the right-state  $(\mathbf{U}_R)$  dependent variables across the control surface are computed by the formula with two accuracy control parameters  $\kappa$  and  $\varphi$ . To achieve the third-order upwind-biased results, the value of  $\kappa$  is set to 1/3 and  $\varphi$  equals unity:

$$\mathbf{U}_L = \mathbf{U}_i + \varphi/4[(1-\kappa)\nabla + (1+\kappa)\Delta]\mathbf{U}_i \tag{2.17}$$

$$\mathbf{U}_{R} = \mathbf{U}_{i+1} + \varphi/4[(1+\kappa)\nabla + (1-\kappa)\Delta]\mathbf{U}_{i}, \tag{2.18}$$

where  $\Delta$  U and  $\nabla$  U denote the forward and the backward differencing, respectively. A fourth-order temporal accuracy is obtained by the Runge-Kutta four-stage method [21,22]:

$$\mathbf{U}^{n+1} = \mathbf{U}^n + \Delta t/6[(\mathbf{U}_t)_1 + 2(\mathbf{U}_t)_2 + 2(\mathbf{U}_t)_3 + (\mathbf{U}_t)_4]. \tag{2.19}$$

All computed results therefore have a third-order spatial and fourth-order temporal accuracy.

## 3 Microwave attenuation in waveguide

In the frequency spectrum of experimental microwave diagnostics  $\varpi_p < \varpi$ , the measured phase shift depends only upon the electron density and the attenuation depends on both density and collision frequency for momentum transfer [11]. For a transverse plane electromagnetic wave in the TE<sub>1,0</sub> mode and traveling in the z direction of a square waveguide, the motion is described by  $E = E_o \exp\left[-\alpha z + i(\beta z - \varpi t)\right]$ , where  $\alpha$  and  $\beta$  are the attenuation and phase constants [23]. The phase constant is given by the relationship of  $\beta = 2\pi/\lambda$ , and the phase velocity of the wave is  $u_{ph} = \varpi/\beta$ . The attenuation and phase constants  $\alpha$  and  $\beta$  of the transverse wave in a rectangular waveguide can be calculated by the following formula:

$$\alpha = (n\pi/a)^2, \qquad \beta = \{(\beta_o^2 + [\beta_o^4 - (\sigma/c\varepsilon)^2]^{1/2})/2\}^{1/2},$$
 (3.1)

where  $\beta_o = [(\varpi/c)^2 - (n\pi/a)^2]^{1/2}$ , c is the speed of light, and a is the characteristic length of the waveguide. In the wavelength range where the incident microwave has a higher

frequency than the plasma, the plasma becomes a relatively low-loss dielectric medium. The wave amplitude attenuates exponentially and the phase shifts linearly proportional the distance propagated [23]. However, there are serious limitations of applying the one-dimensional, plane-wave model for plasma diagnostics that has a finite dimension and fluctuating geometries. Added to these limitations, the unknown effects of wave diffractions and reflections at the media interfaces and the refraction from the divergent wave are problem dependent and in general not assessable.

To better understand the underlying physics of a reflected microwave at the interfaces, computing simulations are performed to analyze the reflection at the media interfaces. All numerical results are presented in the non-dimensional abscissas z, normalized by the wavelength. The computational simulation for a traveling microwave in homogeneous, isotopic plasma has been developed by earlier research efforts [21, 22]. In Fig. 2, the x component of the magnetic field intensities  $B_x$  over a range of electrical conductivities at fixed values of microwave frequency and plasma electric permittivity are given together with theoretical results,  $0.0 < \sigma/\varpi\varepsilon < 0.25$ . The simulated microwave in the transverse electrical  $TE_{1,0}$  mode is propagating through the plasma at a frequency of 4.0 GHz and a wavelength of 7.495 cm. The microwave traveling in plasma that is devoid of media interface reveals a monotonous attenuation proportional to the magnitude of the electric conductivity. By doubling the value of electric conductivity, the wave is completed dissipated in 4.75 wavelengths. The numerical results are in excellent agreement with the theory [23].

Interference of media interface on the transmitted microwave can be dominant particularly when the difference of intrinsic impedances is large and the plasma is only a few wavelengths in thickness. This type of plasma dimension is frequently encountered in most plasma flow channels [15,16,20,24]. This interference effect can easily obscure the plasma absorption. In addition, if the microwave wavelength is comparable to the plasma thickness, diffraction and surface waves around the discharge are also possible. These effects can be more pronounced than the absorption.

For plasma sheet with a finite thickness and with a sharp boundary, the reflection of the microwave at the boundary always takes place because of the mismatched intrinsic impedance of two media. The refraction occurs both at the incident and exiting interfaces and affects measurements. This phenomenon is clearly demonstrated by numerical simulation of a guided  $TE_{1,0}$  microwave with a frequency of 4 GHz. All the following numerical results are obtained on a  $(25\times25\times197)$  grid system. The entire computational domain consists of 10 wavelengths and the square waveguide has sidewall dimensions of one wavelength each. The plasma sheet strides the guided wave at the middle point of the waveguide and has a thickness of two wavelengths. The plasma sheet is characterized by a uniform and greater electrical conductivity,  $\sigma = 0.75\varpi\varepsilon$ .

The  $TE_{1,0}$  wave has only two magnetic field components  $H_x$ ,  $H_z$  and a sole electric displacement component  $D_y$ . In Fig. 3, the x component of the magnetic field strength along the microwave path is presented. For purpose of comparison, the same variable in free space is pended in the figure as a reference. Both waves travel from the coordinate

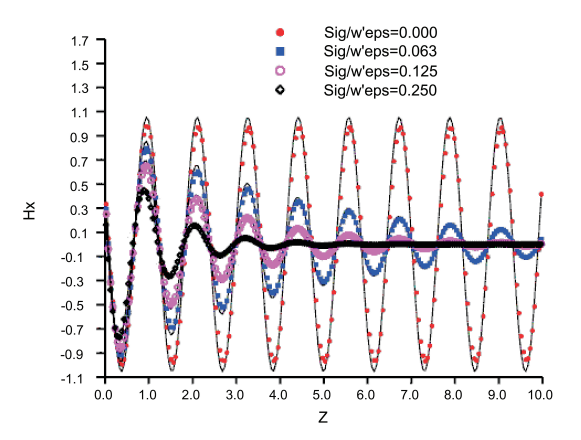


Figure 2: Microwave attenuation in isotopic plasma. Red:  $\sigma/\varpi\varepsilon=0$ ; blue:  $\sigma/\varpi\varepsilon=0.063$ ; pink:  $\sigma/\varpi\varepsilon=0.125$ ; and black:  $\sigma/\varpi\varepsilon=0.25$ .

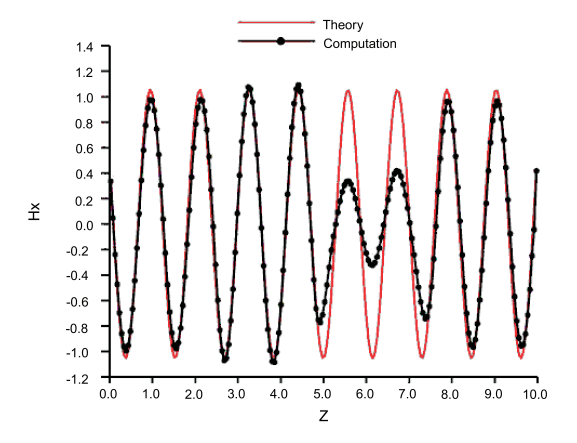


Figure 3: Magnetic field of microwave in plasma sheet. Red: free space; black: computation.

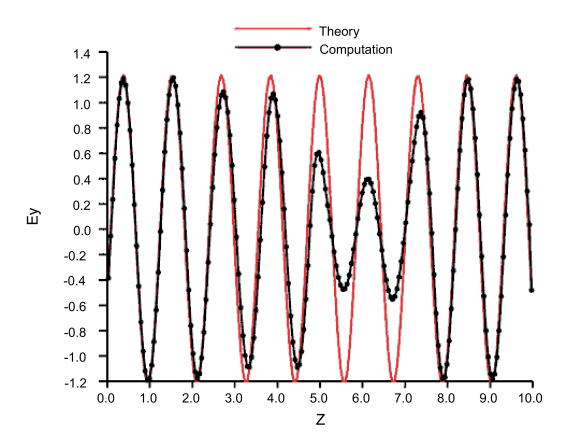


Figure 4: Electric field of microwave in plasma sheet. Red: free space; black: computation.

origin and sample at the identical time interval. From the numerical results, the magnetic field is substantially distorted by the reflections from the media interfaces. This behavior is drastically different than the numerical results describing the microwave motion that is completely confined in the plasma. Under that circumstance, the reflected wave does not exist and the wave attenuation is continuous and persistent through the entire computational domain.

The reflected wave from the incident interface produces a wave cancellation toward its origin. In the plasma domain, the microwave magnetic component exhibits a significant distortion, and remerges at the exit interface to show attenuation in wave amplitude. This interference has been known to obscure the plasma absorption measurements [11], and is demonstrated by the present numerical simulation. The microwave propagated in a single medium and used as a reference beam for comparison actually indicates a phase shift of the microwave that travels through the plasma with only a distance of two wavelengths.

The y component of the electrical field intensity of the  $\text{TE}_{1,0}$  wave is depicted in Fig. 4. Again the reflected wave from the media interfaces substantially distorts the electrical field of the microwave in direct contrast to the microwave propagating in the plasma without interface boundaries. For the electrical field component, the reflected wave from the incident media interface exhibits a much more pronounced phase shift and amplitude reduction.

Since the Poynting vector,  $\mathbf{P} = \mathbf{E} \times \mathbf{H}$ , in the electromagnetic field is a measure of the instantaneous rate of energy flow per unit area at that point and the direction of energy flow is perpendicular to E and H, it is the basic measurement of microwave attenuation [11–13, 23]. For the transverse electric  $TE_{1,0}$  wave, the Poynting vector can be given as:

$$\mathbf{P} = -E_z H_y \mathbf{i} - E_x H_z \mathbf{j} + (E_x H_y - E_y H_x) \mathbf{k}. \tag{3.2}$$

The magnitudes of the Poynting vector of  $TE_{1,0}$  electromagnetic waves at an instance are presented in Fig. 5. This quantity in a constant cross-section square waveguide can be viewed as the dynamic range of the electromagnetic energy flux. As before, this figure only presents the results of two values of the parameters  $\sigma/\omega\xi$  of 0.0 and 0.25. In the dielectric medium ( $\sigma=0$ ), the magnitude of the Poynting vector maintains a constant value, as it should. The magnitude of the energy flow diminishes by dissipation as the electric conductivity of the medium has a finite value [21,22]. In the thin plasma sheet the Poynting vector exhibits drastically adjustments to the refractions from the media interfaces and yields uniform attenuation toward the exiting computational domain. The total energy conveyed by the microwave shall be the integrated result over the entire waveguide and over at least one period of wave motion, in the present discussion only a sampling along the guided wave is depicted to highlight the discussion.

The overall behavior of the guided microwave as it penetrated a plasma sheet with a distance of two wavelengths is given in Fig. 6. For the purpose of a simple illustration, different components of the guided wave are projected onto the upper (electric displacement) and lower (magnetic flux density) surface. The electric displacement is also included on the far-side wall to show the planer-wave structure of the TE<sub>1,0</sub>wave. The overall field

structure substantiates the observation that the reflections from the media interfaces create a very complex wave structure within the plasma sheet, but the attenuated microwave still retains most of its incident wave characteristics. Since the microwave measurement is an integrated result from the beam path, it reflects only an accumulated effect. The measurement is therefore sampling condition dependent; no general conclusion can be drawn to compensate the effects of reflection.

#### 4 Microwave antenna

A key element of plasma diagnostics using microwave probing is a pair of pyramidal horns. Their main function is to collimate the microwave beam and to transmit and receive a microwave across a plasma medium [11–13]. The transport property of the weakly ionized gas is deduced from the accumulated microwave energy loss along the beam path by absorption. For accurate data reduction, the measurement may need to address the wave reflection and diffraction at multiple media interfaces [17–20]. Therefore, the numerical simulation must be built on the ability to predict the microwave dissipation and dispersion as it propagates in an electrically conducting medium. In particular, the numerical simulation also requires analyzing the electromagnetic wave propagation entering and exiting the pyramidal horns. All these capabilities will be eventually assembled to accomplish the complete simulation of the microwave diagnostics for ionized gas.

A pyramidal horn generally has a rectangular cross section; at the exit plane of the horn (aperture), the height and the width of the horn are enlarged by a given ratio [31–33]. Again in application, only the electromagnetic wave in the  $TE_{1,0}$ mode is used, because this wave has the lowest cutoff frequency of any higher order mode [23]. In applications focused on radiating structures, the pyramidal horn is mostly utilized as a feed for reflectors and lenses, but it is also a common element of phased arrays. For this reason, the overall performance of an antenna system is often judged by its beam width and/or its directivity. However in plasma diagnostics, the total field radiated by a horn must utilize a combination of the direct field and the diffractions from the edges of its aperture. For computational microwave diagnostics, the horn edge diffraction together with the far-field boundary offers additional challenges.

The microwave transmission is simulated at a frequency of 12.5 GHz ( $\lambda$ =2.398cm). The entrance of the pyramidal horn has the dimension in wavelengths of (0.397 × 0.928), the smallest and the normalized length scale is 0.397 wavelengths (0.938cm). The horn increases its cross section linearly; its aperture has the dimensions in wavelengths of (3.045 × 3.640). The total length of the horn is 3.307 wavelengths. For the present investigation, two groups of computations for the microwave antenna were conducted. For each group of simulations, a single mesh system was utilized.

The challenge to an electromagnetic radiating structure simulation lies in the far-field boundary condition that is also the inherent difficulty for computational electromagnetics [29,30,32,33]. The most popular approaches in the computational electromagnetics

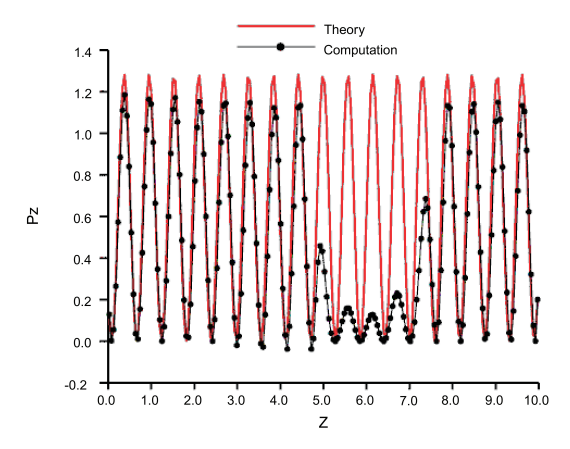


Figure 5: Poynting vector of microwave in plasma sheet. Red: free space; black: computation.

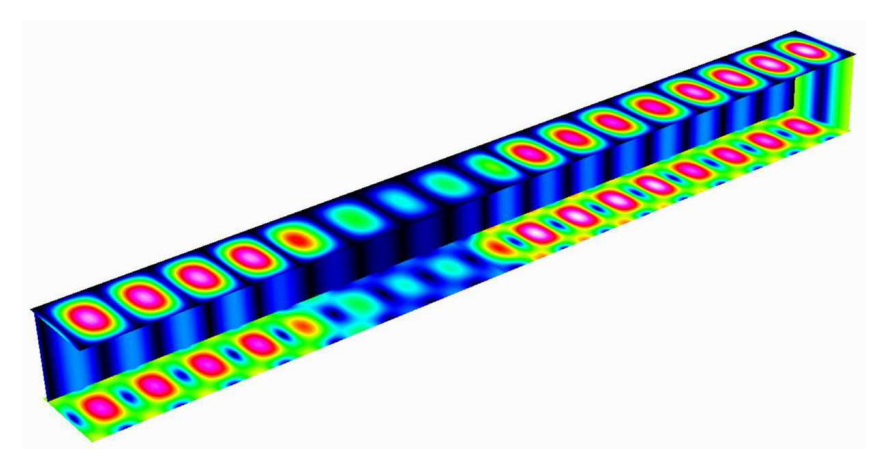


Figure 6: Electromagnetic field structure of guided microwave.

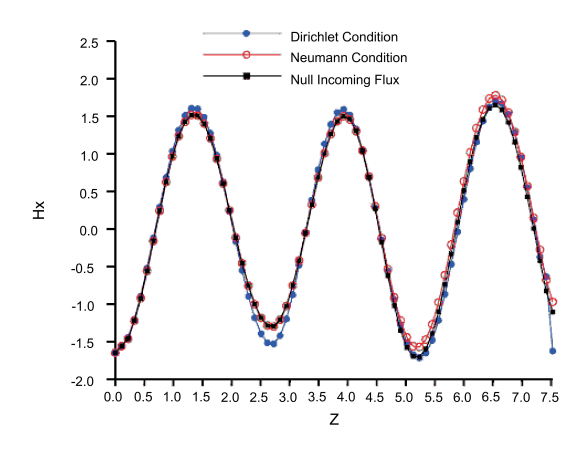


Figure 7: Far-field boundary conditions of antenna. Blue: Dirichlet condition; red: Neumann condition; black:  $\frac{1}{2}$  null incoming flux.

community are the absorbing boundary condition and the perfectly matched-layer scheme [32,33]. The latter is actually derived from the characteristics or the domain of dependence of the hyperbolic partial differential equations system [30]. In the present split flux vector formulation, this far-field boundary condition is implemented by setting the incoming flux vector component to a null value,  $\mathbf{F}_{\zeta}^{-} = 0$ , equations (2.14) and (2.16).

A mesh system of  $(73 \times 25 \times 71)$  is adopted for all computations within the pyramidal horn. The results from different far-field boundary conditions at the aperture of the pyramidal horn are summarized in the following. Since the basic behavior of the magnetic and the electrical components are similar, only the computed  $H_x$  is given in Fig. 7. Three different boundary conditions are examined; the first calculation based on the perfect shift condition,  $\mathbf{U}^{n+1}(i,j,k) = \mathbf{U}^n(i,j,k-1)$  for all variables at the horn exit as the prescribed value [21,22]. This condition is exact for a simple windward scheme when the Courant-Friederichs-Lewy (CFL) coefficient is equal to unity. For the present high-resolution windward bias scheme, a small error is noted and actually propagates backward into the pyramidal horn. The Neumann type of boundary condition is also implemented to alleviate the reflected Fourier components at the exit boundary; a discernable improvement is indicated over that of the Dirichlet type. However, the null incoming flux condition,  $\mathbf{F}_{\zeta}^-(i,j,k) = 0$ , produces the best result of all conditions investigated.

The difference between the Neumann type and the null incoming flux boundary conditions at the pyramidal horn is subtle and is demonstrated by the comparison of the contours presentation of the electrical field  $D_y$  in Fig. 8. The calculation using the Neumann condition is depicted in the upper half plane of the horn. The continuous contours of the numerical result using the null incoming flux condition are given in the lower half plane. The basic and main microwave structure is nearly indistinguishable; the minuscule disparities are concentrated beyond the transition region from the planar to spherical wave front within the horn and at the antenna exit plane.

For the complete radiating field, by taking advantage of the symmetrical property with respect to the x coordinate only the upper half space was simulation by a single mesh system of  $(74 \times 5 \times 142)$ . The entire three-dimensional computational domain generated by a surface-oriented coordinate transformation has the normalized physical dimensions with the minimum height of the rectangular waveguide of  $(15.67 \times 6.51 \times 18.80)$ . The grid distribution on the middle plane of the y coordinate is depicted in Fig. 9, for clarity only each other coordinate lines are included. On the body-oriented transformed coordinates, the surfaces of the pyramidal horn and its exit are rest on the constant value coordinate lines. A partial validation of the computed electromagnetic components and the theoretical results within the pyramidal horn has been performed in an earlier effort [22]. Over the entire range of the parameter  $0.0 < \sigma/\omega\xi < 0.25$ , the agreement between the computational and theoretical results is reasonable while the numerical results slightly underpredict the theory by 1.22 percent. The maximum discrepancy between the computed and the theoretical results is detected at the highest value of electrical conductivity. Additional grid density refinement investigation for better numerical resolution has shown a diminished return.

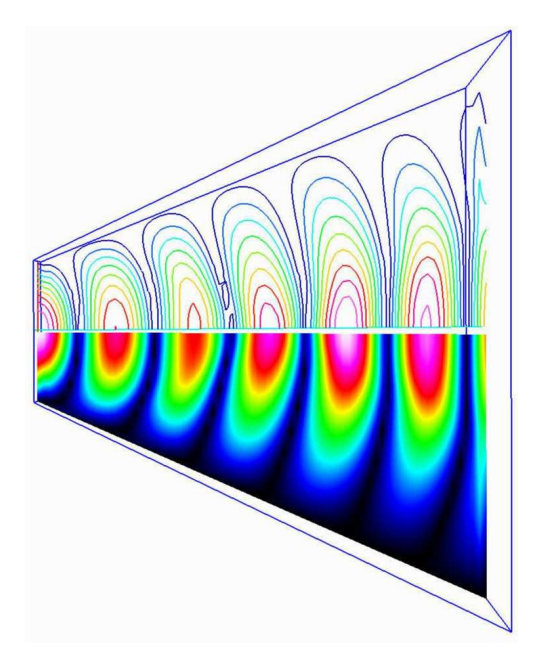


Figure 8: Comparison of electrical fields with different far-field boundary conditions.

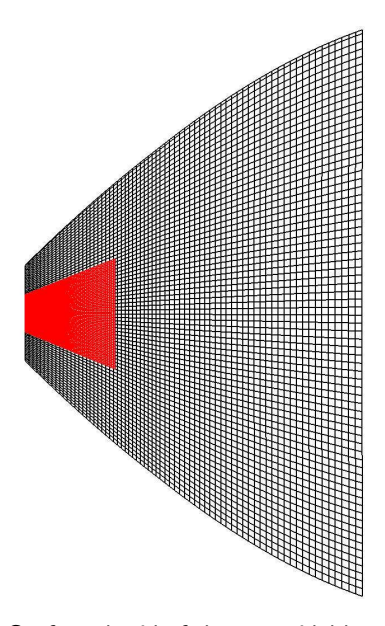


Figure 9: Body-Conformal grid of the pyramidal horn radiating field.

The microwave propagation is strictly a time-dependent phenomenon that may have a periodic asymptote. The temporal sequence of the probing microwave as it propagates from the waveguide to the far-field boundary is presented by its electrical field component,  $D_y$ . Fig. 10(a) shows the microwave begins to emerge from the pyramidal horn into

a quiescent free space. The  $TE_{1,0}$  wave transmitting from the waveguide exhibits the development of a spherical wave front within the pyramidal horn and the wavelength deceases as the wave approaches the antenna exit [32]. As the wave completely exits into the free space, the edge diffraction at the pyramidal horn is clearly indicated, Fig. 10(b). Complex wave refraction also takes place outside of the horn; the numerical result also shows that the reflected wave is not in phase with the emitting microwave and has a different wavelength in free space than that within the waveguide.

Figs. 10(c) and 10(d) depict the microwave as it reaches the halfway point and the outer edge of the computational domain. Three features stand out; first the edge diffraction is persistently presented and the wavelength remains to be a constant and shorter value than that within the antenna. Second, at the far field boundary the microwave front becomes spherical. Finally, the simulated electrical field correctly captures the discontinuous behavior of the electrical displacement  $D_y$ , on the outer surface of an electrically perfect conducting pyramidal horn.

The evolving electrical displacement along the microwave beam path is given in Fig. 11. The time scale in this presentation is given in terms of the number of time steps advanced. The normalized time step increment normalized by speed of light is 0.0308. Because spatial stretching was included in the coordinate generation, the unity CFL condition was not uniformly honored. A systematic progression of the microwave from the waveguide to the far-field boundary without numerical reflection is clearly illustrated.

The entire electromagnetic field, two magnetic field components,  $H_x$  and  $H_z$  and the sole electric field component  $D_y$  along the z coordinate are plotted together in Fig. 12. All field components correctly exhibit diminishing amplitude as the radiating field expands into a greater spherical wave front. The present numerical result also shows that two key components of the Poynting vector,  $H_x$  and  $D_y$ , are completely out of phase from each other. Unfortunately, there is no known experimental available for detailed validation.

The Poynting vectors along the identical z coordinate to that of the electromagnetic field components are depicted at two different time intervals, the time of 9.24 (N=300) and 18.48 (N=600), Fig. 13. At these instants, the microwave has propagated to the halfway and the edge of the computational domain. The Poynting vector along each coordinate ray diminishes accordingly as the area of the wave front expands. The integrated value of the Poynting vectors with respect the projected area and at least one wave period in time shall remain a constant in a dielectric medium. The present numerical results demonstrated a discrepancy on the order of magnitude of  $10^{-2}$  based on the entrance value from the waveguide; this is also the accuracy limit of the present computation. A higher numerical resolution can be achieved by grid density refinement.

## 5 Attenuation in radiating field

In plasma diagnostic experiments, the absorption is measured by the microwave power loss after the microwave has passed through the plasma and been collected by the receiving

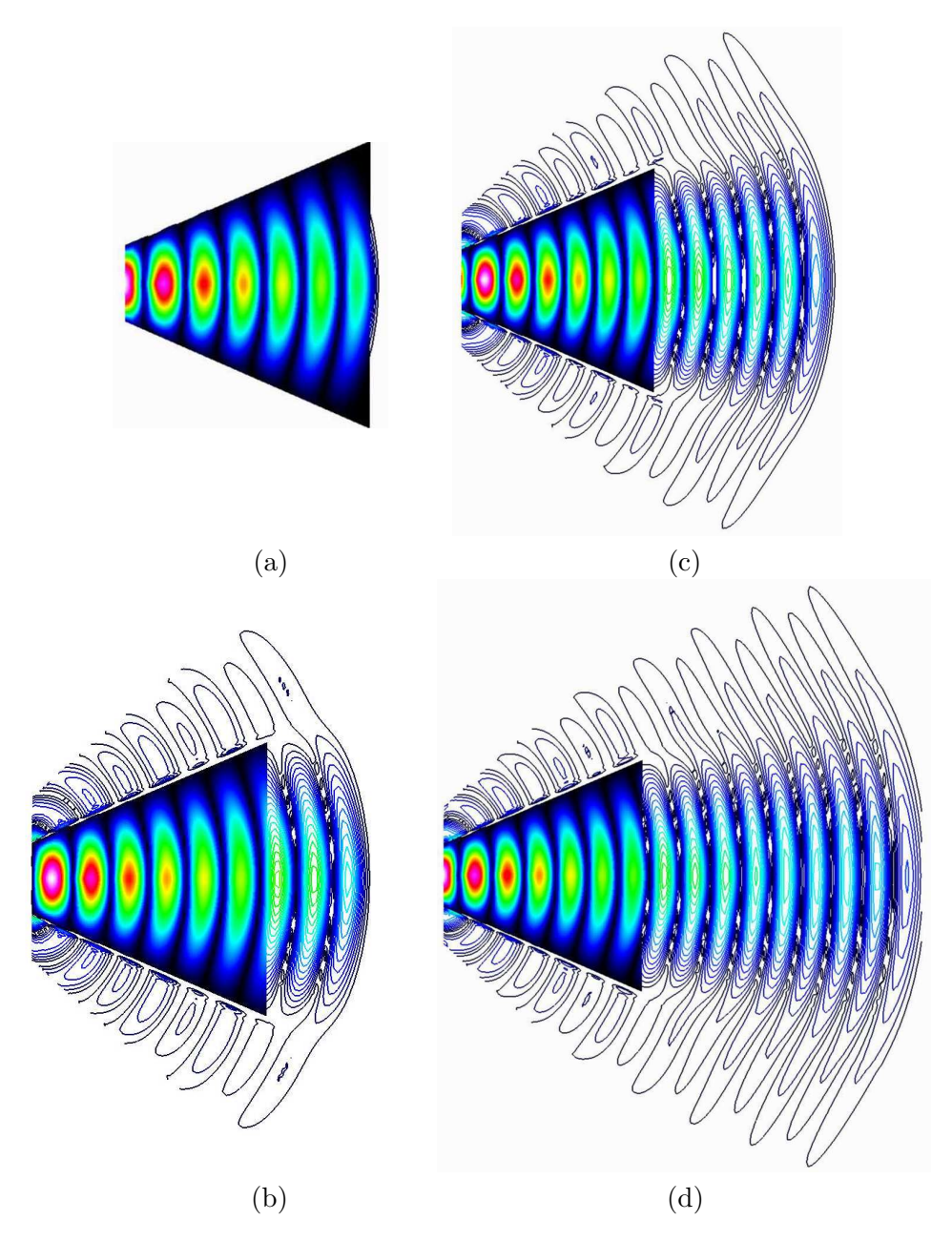


Figure 10: (a) Microwave exits antenna (b) Microwave propagates 6 wavelengths from antenna (c) Microwave propagates 3 wavelengths from antenna (d) Microwave arrives at the computational boundary.

pyramidal horn. In most experiments the microwave power is recorded as an averaged voltage of the wave signal over the beam cross-section and several periods of the probing wave [17–19]. It is also the fundamental bandwidth of the measurement uncertainty, because from the formulation of the Poynting vector the voltage is not necessarily linearly

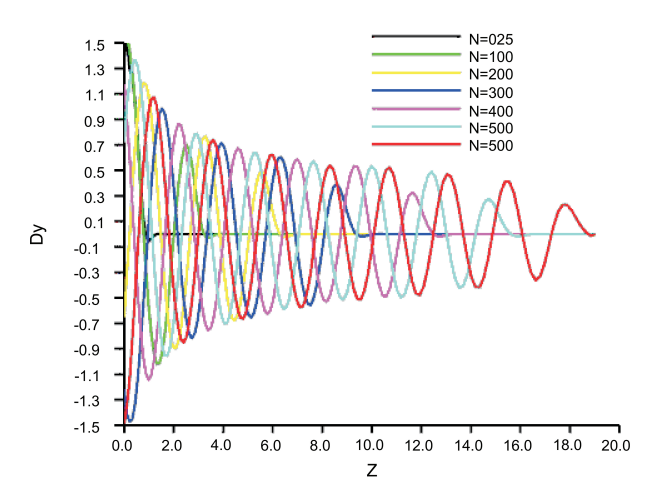


Figure 11: Temporal sequence of electric displacement,  ${\rm D}_y$ . Black: N=25; green: N=100; yellow: N=200; blue: N=300; pink: N=400; light blue: N=500; and red: N=600.

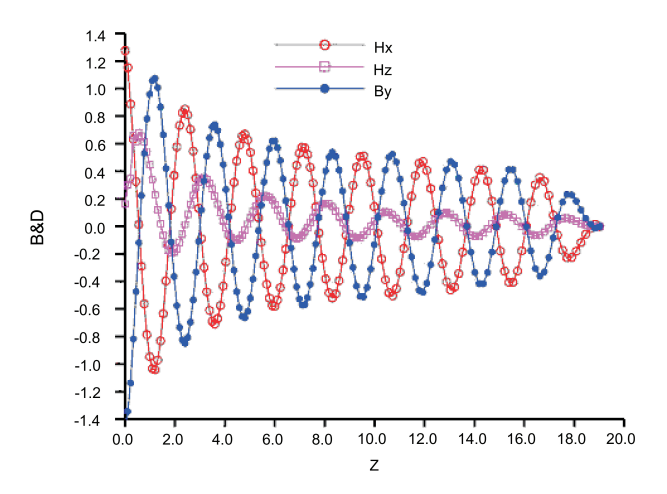


Figure 12: Electromagnetic field in microwave path. Red:  $H_x$ ; pink:  $H_z$ ; and blue:  $H_y$ .

proportional to the microwave power. Most importantly, the recorded data are the accumulative information along the beam path and assumes the plasma has a uniform property. The present computing result conforms to this condition, but the edge diffraction from the pyramidal horn and the wave reflections from the media interfaces are included in the simulation.

Once the computational simulation capability is developed for the radiating field of a microwave antenna, the attenuation of the wave penetrating through plasma can be analyzed by a comparative study. In the present investigation, directly supporting to experimental efforts, only plasma sheets less than one and one-half wavelength depths are

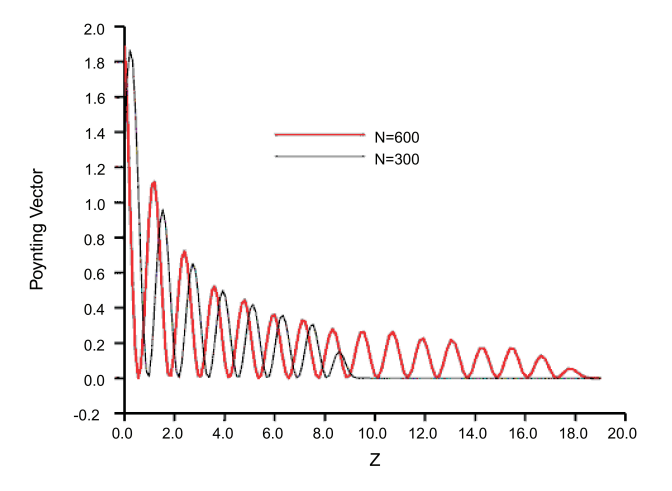


Figure 13: Poynting vector in microwave path. Red: N=600; and black: N=300.

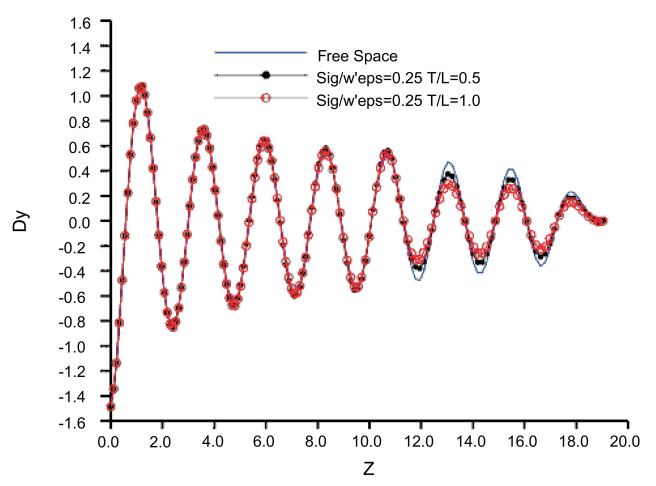


Figure 14: Microwave electrical displacement in radiating field. Blue: free space; black:  $\sigma/\varpi\varepsilon=0.25$  and T/L=0.5; red:  $\sigma/\varpi\varepsilon=0.25$  and T/L=1.

simulated [20, 24]. The difficult issues of analyzing non-uniform plasma domain require both greater numerical resolutions in time and space, as well as, a solid validating database. These challenges need to be met for a better understanding of the important physical phenomena.

In Fig. 14, the instantaneous electric displacement  $D_y$  along the z coordinate is given. The result of microwave radiating into the free space ( $\sigma=0$ ) and results of microwaves subsequently propagating through uniform and sharp edge plasma sheets of different thicknesses are presented together (T/L=0.5 and 1.0 or  $T/\lambda=0.275$  and 0.55). The plasma sheets are assigned to have the identical transport property with a value of  $\sigma/\varpi\varepsilon=0.25$ . In the radiating field where the microwaves expand continuously, the amplitude of the elec-

tromagnetic field intensities decrease accordingly. All simulated waves exiting the antenna at the location z/a=7.704, on this graphical scale, the edge diffraction of the antenna is not discernable. However, the reflected wave from the front edge of the plasma sheet is detected and the effect of the reflected to the incident wave appears to be minuscule. For both plasma sheets simulated, the front edge of the plasma sheet is located at the distance of z/a=10.955 from the pyramidal horn entrance. The attenuation of the electric displacement of the microwave is greater for the wave penetrating through the thicker plasma sheet.

The instantaneous Poynting vectors of three simulations along a z coordinate are depicted in Fig. 15. In the continuously expanding structure of radiation, the Poynting vector no longer represents the dynamic range of the transmitting energy as in a constant cross-section waveguide, because the energy flux density decreases with the increasing cross section of beam path. However, the different attenuations of the radiating microwaves along different beam paths are demonstrated. The microwave that passes through the thicker plasma sheet suffers the greater lost of electromagnetic energy than the thinner sheet. In all plasma diagnostics using microwaves, even if the transport property remains unaltered, the fluctuating plasma still can change its dimension and geometric boundary constantly. Under this circumstance, the measurement accuracy is seriously challenged.

The spatially averaged Poynting vector over the entire beam cross section from the antenna entrance to the outer edge of the computational domain is presented in Fig. 16. First, insufficient numerical resolution becomes clearly evident in direct contrast to the guided microwave simulation. Although the electromagnetic wave in the  $TE_{1,0}$  mode is a linearly polarized plane wave, the sparse cell density in the y coordinate direction fails to produce sufficient resolution for the area integration. The spatially integrated Poynting vector therefore is used in here to show only the global behavior of the microwave attenuation through plasma sheets of different thickness.

For the first time, the edge diffraction at the exit of the pyramidal horn can be clearly observed, at the distance of z/a=7.704 from the antenna entrance. The diffraction induces a perturbation of the Poynting vector locally and propagates toward the plasma sheet. Unfortunately, the quantification of the diffraction to the quality of the signature is not obtainable. The reflected waves from the front edge of plasma with different thickness affect the incident wave identically as it should, because the reflected waves are resulting only from the mismatched intrinsic impedance at the media interfaces and are independent of the thickness of the plasma.

Finally, and most importantly, the thickness of the plasma sheet has shown a profound effect on the microwave attenuation. At the microwave probing frequency of 12.5 GHz and the plasma property characterized by the parameter of  $\sigma/\varpi\varepsilon=0.25$ , attenuation by a plasma sheet with a thickness of 0.55 wavelengths is in a range of 65 % greater than that of the thinner sheet with a thickness of 0.275 wavelengths. The Poynting vector of the probing microwave losses nearly half of its dynamic range when it passed through these plasma sheets with a thickness no more than one-half the probing wavelength.

In practical applications, the diffraction and refraction of the probing beam and plasma

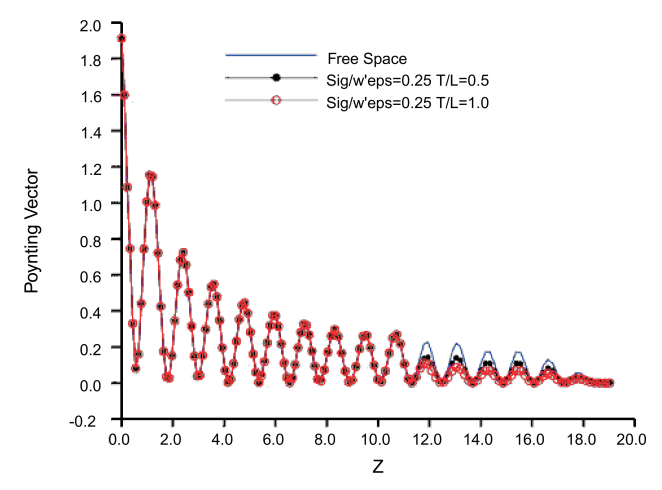


Figure 15: Poynting vector in radiating field. Blue: free space; black:  $\sigma/\varpi\varepsilon=0.25$  and T/L=0.5; red:  $\sigma/\varpi\varepsilon=0.25$  and T/L=1.

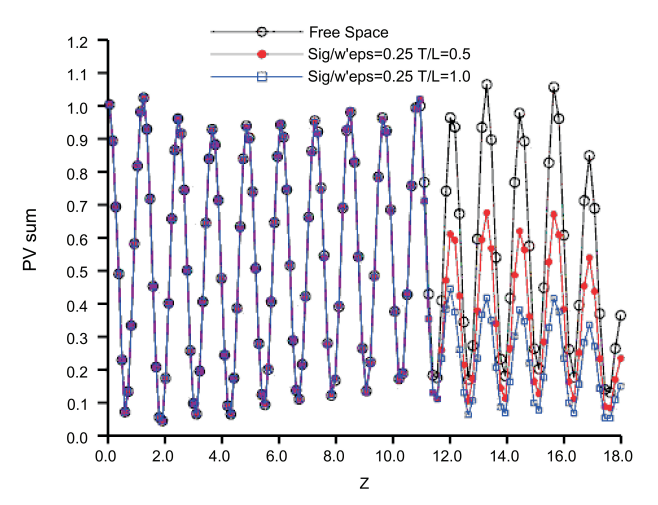


Figure 16: Dynamic range of spatial averaged Poynting vectors. Blue: free space; black:  $\sigma/\varpi\varepsilon=0.25$  and T/L=0.5; red:  $\sigma/\varpi\varepsilon=0.25$  and T/L=1.

are unaccounted at the present. These issues of practical application interest and accurate assessment of experimental measurements will be persistently pursued.

# 6 Concluding remarks

The numerical analysis for microwave attenuation in plasma diagnostics has reached a stage that the microwave radiating from a pyramidal horn and passing through a thin plasma sheet can be simulated. The microwave attenuation in a waveguide is easily observed with increasing electrical conductivity and the thickness of plasma sheet. At a

microwave frequency of 4.0 GHz, when the non-dimensional electrical conductivity,  $\sigma/\varpi\varepsilon$ , of a simulated homogeneous, isotopic plasma increase from 0.125 to 2.50, the wave is completely dissipated from 10 to 4.75 wavelengths. The numerical simulations reveal the edge diffraction at the exit of pyramidal horn and its effect to wave attenuation is less important than the reflected wave that originates from the interface of the media.

The dynamic range of the spatially averaged Poynting vector reduces sharply along the beam path when the probing microwave passed through thin plasma sheets. The reduced magnitude is proportional to the thickness of plasma sheets. At a probing microwave frequency of 12.5 GHz and the plasma sheet characterizing by the parameter of  $\sigma/\varpi\varepsilon = 0.25$ , the range reduces by a value of 65% with a 55% thinner plasma sheet.

In a guided microwave, the reflected waves from the front and the back edge of a plasma sheet induced by the mismatched intrinsic impedances generate a drastic distortion of the electromagnetic wave structure within the plasma sheet. The attenuation of the passing microwave at a lower microwave frequency is still strongly dependent on the electrical conductivity and the permittivity of the plasma than the reflection from the media interface.

These research findings have been productively applied to the better understanding and accurate interpretation of experimental data from a hypersonic plasma channel. The basic issue still remains in the separation of complex microwave physics and possible numerical artifacts.

### Acknowledgments

The sponsorship from Dr. J. Schmisseur and Dr. F. Fahroo of the Air Force Office of Scientific Research is deeply appreciated. The stimulating discussions with Prof. J. Menart of Wright State University, as well as, Dr. R. Kimmel and J. Hayes of the Air Force Research laboratory are sincerely acknowledged.

#### Nomenclature

- **B** Magnetic flux density,  $\mathbf{B} = \mu \mathbf{H}$
- c Speed of light
- E Electric field intensity
- H Magnetic field Strength
- P Poynting vector
- U Dependent variables
- $\lambda$  Wavelength
- $\xi, \eta, \zeta$  Transformed curvilinear coordinates
  - $\sigma$  Electric conductivity

- C Coefficient matrix
- **D** Electric displacement,  $\mathbf{D} = \varepsilon \mathbf{E}$
- F Flux vector
- J Electric current density
- T Thickness of plasma sheet
- $\varepsilon$  Electric permittivity
- $\mu$  Magnetic permeability
- $\rho$  Surface charge density
- $\overline{\omega}$  Frequency

#### References

- [1] J. S. Shang, Historical perspective of magneto-fluid-dynamics, in: Introduction to Magneto-Fluid-Dynamics for Aerospace Applications, Lecture Series 2004-01, von Karman Institute for Fluid Dynamics, Rhode-ST-Genese Belgium, Oct. 2003.
- [2] J. S. Shang, MFD research in US toward aerospace applications, in: Introduction to Magneto-Fluid-Dynamics for Aerospace Applications, Lecture Series 2004-01, von Karman Institute for Fluid Dynamics, Rhode-ST-Genese Belgium, Oct. 2003.
- [3] J. R. Roth, Electrohydrodynamic flow control with a glow-discharge surface plasma, AIAA J., 38(7) (2000), 1166-1172.
- [4] G. Artana, J. Adamo, L. Leger, E. Moreau and G. Touchard, Flow control with electrohydrodyamic actuators, AIAA J., 40(9) (2002), 1773-1779.
- [5] C. L. Enloe, T. E. McLaughlin, R. D. Van Dyken, K. D. Kachner, E. J. Jumper and T. J. Corke, Mechanisms and responses of a single dielectric barrier plasma actuator: Plasma morphology, AIAA J., 42 (2004), 589-594.
- [6] J. S. Shang and S. T. Surzhikov, Magnetoaerodynamic actuator for hypersonic flow control, AIAA J., 43(8) (2005), 1633-1643.
- [7] Y. Kolesnichenko, Basics in beams MW energy deposition for flow/flight control, AIAA 2004-0669, Reno NV, 2004.
- [8] C. Park, U. B. Mehta and D. W. Bogdanoff, MHD energy bypass scramjet performance with real gas effects, J. Propul. Power, 19(5) (2001), 1049-1057.
- [9] R. B. Miles, G. L. Brown, W. R. Lempert, R. Yetter, G. L. Williams, S. M. Bogdonoff, D. Natelson and J. R. Guest, Radiatively driven hypersonic wind tunnel, AIAA J., 33(8) (1995), 1463-1470.
- [10] N. Anikin, E. Kukaev, S. Starikovskaia and A. Starikovskii, Ignition of hydrogen-air and methane-air mixtures at low temperatures by nanosecond high voltage discharge, AIAA 2004-0833, Reno NV, January 2004.
- [11] M. A. Heald and C. B. Wharton, Plasma Diagnostics with Microwaves, John Wiley and Sons, New York, 1965.
- [12] V. E. Golant, Methods of diagnostics based on the interaction of electromagnetic radiation with a plasma, in: A. Galeev and R. Sudan (Eds.), Basic Plasma Physics I, North Holland Publishing Co., Amsterdam, 1983, pp. 630-680.
- [13] W. Lochte-Holtgreven (Ed.), Plasma Diagnostics, North Holland Publishing Co., Amsterdam, 1968.
- [14] Yu. P. Raizer, Gas Discharge Physics, Springer-Verlag, Berlin, 1991.
- [15] J. S. Shang, R. Kimmel, J. Hayes, C. Tyler and J. Menart, Hypersonic experimental facility for magnetoaerodynamic interactions, J. Spacecraft Rockets, 42(5) (2005), 780-789.
- [16] R. Kimmel, J. Hayes, J. Menart, S. Shang, S. Henderson and A. Kurpik, Measurements of a transverse DC discharge in a mach 5 flow, AIAA 2003-3855, Orlando, FL, 23-26 June 2003.
- [17] L. D. Smoot and D. L. Underwood, Prediction of microwave attenuation characteristics of rocket exhausts, J. Spacecraft Rockets, 3(3) (1966), 302-309.
- [18] R. A. Fedrick, J. A. Blevins and H. W. Coleman, Investigation of microwave attenuation measurements in a laboratory-scale motor plume, J. Spacecraft Rockets, 32(5) (1995) 923-925.
- [19] I. Funaki, H. Ogawa, T. Kato, T Abe, K. Fujita and S. Nonaka, Microwave attenuation measurement of full-scale solid rocket motor plumes, AIAA 2002-2241, Maui Hawaii, May 2002.

- [20] A. Kurpik, J. Menart, J. Shang, R. Kimmel and J. Hayes, Technique for making microwave absorption measurements in a thin plasma discharge, AIAA 2003-3748, Orlando, FL, 23-26 June 2003.
- [21] J. S. Shang, Computational electromagnetics for microwave attenuation in weakly ionized air, AIAA 2003-3621, Orlando, FL, 23-26 June 2003.
- [22] J. S. Shang, Simulating microwave diagnostics for weakly ionized gas, AIAA 2004-0676, Reno NV, January 5-8, 2004.
- [23] J. D. Krause, Electromagnetics, McGraw-Hill, 1953, pp.390-481.
- [24] S. Henderson, J. Menart, J. S. Shang, R. Kimmel and J. Hayes, Data reduction analysis for a cylindrical, double langmuir probe operating in a high speed flow, AIAA 2004-0360, Reno NV, January 5-8, 2004.
- [25] S. T. Surzhikov and J. S. Shang, Two-component plasma model for two-dimensional glow discharge in magnetic field, J. Comput. Phys., 199(2) (2004), 437-464.
- [26] J. Menart, J. Shang, R. Kimmel, and J. Hayes, Effects of magnetic fields on plasmas generated in a mach 5 wind tunnel, AIAA 2003-4165, Orlando, FL, 23-26 June 2003.
- [27] M. Mitchner and C. H., Jr. Kruger, Partially ionized gases, John Wiley & Sons, NY, 1973, pp. 126-241.
- [28] N. G. Van Kampen and B. U. Felderhof, Theoretical Methods in Plasma Physics, North-Holland Publishing Co., Amsterdam Netherlands, 1967, pp.101-129.
- [29] J. S. Shang, Characteristic-based algorithms for solving Maxwell equations in the time domain, IEEE Antennas Propag., 37(3) (1995), 15-25.
- [30] J. S. Shang, Shared knowledge in computational fluid dynamics, electromagnetics, and magneto-aerodynamics, Prog. Aerosp. Sci., 38(6-7) (2002), 449-467.
- [31] C. A. Balanis, Antenna Theory: Analysis and Design, John Wiley & Sons, New York, 1982, pp. 8-3, 8-86.
- [32] J. Maloney, G. Smith, E. Thiele and O. Gandhi, Modeling of antennas, in: A. Taflove and S. Hagnes (Eds), Computational Electromagnetics: The-Finite-Difference, Time-Domain Methods, second ed., Artech House, Boston, 2002, pp. 627-701.
- [33] D. Katz, M. Piket-May, A. Taflove and K. Umashankar, FDTD analysis of electromagnetic wave radiation from systems containing horn antennas, IEEE T. Antenn. Propag., 39(8) (1991), 1203-1212.